frontiers | Frontiers in Materials

TYPE Original Research
PUBLISHED 17 January 2023
DOI 10.3389/fmats.2023.1120520

OPEN ACCESS

EDITED BY
Xinpeng Wang,
Qingdao University of Technology, China

REVIEWED BY
Ping Duan,
China University of Geosciences Wuhan, China
Juntao Ma,
North China University of Water Conservancy and Electric Power, China
Rui Yu,
Wuhan University of Technology, China

*CORRESPONDENCE
Tong Lv,
930732405@qq.com

SPECIALTY SECTION
This article was submitted to Computational Materials Science, a section of the journal Frontiers in Materials

RECEIVED 10 December 2022
ACCEPTED 04 January 2023
PUBLISHED 17 January 2023

CITATION
Zhang J and Lv T (2023), Hydration and durability of low-heat cementitious composites for dam concrete: Thermodynamic modeling and experiments.
Front. Mater. 10:1120520.
doi: 10.3389/fmats.2023.1120520

Hydration and durability of low-heat cementitious composites for dam concrete: Thermodynamic modeling and experiments

Juntao Zhang and Tong Lv*

State Key Laboratory of Hydraulic Engineering Simulation and Safety, Tianjin University, Tianjin, China

To demonstrate the superiority of dam concrete, a systematic study was conducted to examine the durability of low-heat cementitious composite (LHCC) that is composed of Portland cement (PC), fly ash (FA), and MgO expansive additive (MEA) with PC as the reference group. Through GEMS software, XRD, SEM, and EDS, the difference mechanism in durability between the two cementitious materials was revealed from the perspectives of phase evolution and microstructural characteristics. Water at 40 °C was adopted for curing in the study to match the long-term temperature field inside the concrete dam. According to the results of the RCM, accelerated carbonation, and rapid freeze–thaw cycle experiments, LHCC outperforms PC in durability. The hydration process of LHCC is simulated by inputting the reaction degree of each phase calculated using the MPK model into the GEMS software. The thermodynamic model output shows that portlandite first increases and then decreases as LHCC hydration proceeds, and C-S-H and stratlingite are supplemented in the later stage, which reflects the high performance of FA involved in hydration. In addition, hydrotalcite that is capable of chloride ion adsorption is increasingly generated with the consumption of brucite. As is clearly shown in the SEM images, there are denser space grids formed by overlapping C-S-H in LHCC with almost no capillary pores. Meanwhile, when combined with the results of EDS, it is strongly demonstrated that the FA in LHCC can be hydrated to produce dense fibrous C-S-H in large amounts, providing a basis for the positive development of durability.

KEYWORDS

dam concrete, low-heat cementitious composite, hydration, durability, thermodynamic modeling

Introduction

The construction of water conservancy and hydropower projects is inseparable from mass concrete retaining dams (Wang et al., 2018). Compared with earth-rock dams, concrete dams are more commonly constructed due to their adaptability to various environmental conditions and convenient construction (Noroozi et al., 2022). However, the existence of cement hydration heat makes the temperature in concrete dams reach as much as 70 °C, and it is difficult for the heat stored in the dam to dissipate (Atiş, 2002; Chen et al., 2017; Klemczak et al., 2017). The considerable thermal stress makes the concrete dam susceptible to cracking, which shortens its service life (Tayade et al., 2014). Therefore, it is essential to prevent the cracking of concrete dams in engineering practice.

To mitigate the temperature increase that plays a key role in the prevention of fracture evolution, physical cooling methods are adopted during construction (Ha et al., 2014). For

example, a common practice is to reduce the temperature of the mixture before mixing the concrete or installing pipes for the transfer of cold water into the poured mass concrete, which requires complex construction technology and increases time and economic costs. In contrast, the replacement of cement with FA in large amounts can effectively suppress the generation of hydration heat and facilitates proper construction (Zhang and Canmet, 1995; Ng and Justnes, 2016). With the extension of curing, the pozzolanic activity of FA gradually increases, and secondary hydration occurs with cement. This results in the generation of more and more stable C-S-H, which significantly enhances the performance of dam concrete in crack resistance (Ali and Mullick, 1998; Qian et al., 1998; Wang et al., 2020). Furthermore, in considering the reduction of carbon emissions from the cement industry and the promotion of industrial solid waste recycling, FA has basically been applied as the fifth component of dam concrete (Yoon et al., 2002; Vargas and Halog, 2015).

In reality, it is impossible to completely avoid cracking through controls of the temperature. Cement-based cementitious materials are prone to shrinkage in various ways, such as self-shrinkage, drying shrinkage, plastic shrinkage, and carbonation shrinkage (Wolterbeek et al., 2021; Zheng et al., 2022). In addition to provide channels for harmful ions to pass through, the cracks caused by thermal stress and volume shrinkage can also have negative effects on the properties of cement (Xin et al., 2018). To repair cracks as much as possible, MEA is often added into the dam concrete (Gao et al., 2008). MEA is characterized by a slow hydration process, stable hydration products, and a lasting expansion effect, which matches the long-term temperature drop and volume shrinkage process of hydraulic mass concrete (Mo et al., 2014; Zhang, 2022). As a result, the low-heat cement-based composites obtained by the hydration of cement and large amounts of FA and MEA after mixing have gradually been applied as the major cementitious component of dam concrete (Gao et al., 2013).

To explore the superiority of LHCC, there have been many studies conducted to experiment on its various properties. Choi et al. (2014) conducted tests to confirm that light-burned MgO can improve the compressive strength and durability of FA concrete cured at 20 °C in water over a long time. By measuring the volume deformation of MgO-based shrinkage-compensating cement containing FA, Zhang et al. (2022) found out that FA can help enhance the effectiveness of MEA in compensating for the early shrinkage of cement and suppressing the late excessive delay expansion of $Mg(OH)_2$, which significantly reduces the risk of expansion-induced cracking for the cementitious matrix. These studies have proven the superior influence of FA and MEA on performance despite a lack of clarity on the related hydration mechanism. Meanwhile, prior studies are based on the curing at 20 °C, which is inconsistent with the high-temperature environment inside dam concrete (Dung and Unluer, 2021; Cao and Al-Tabbaa, 2022).

A literature review showed that the long-term internal temperature of mass concrete is approximately 40 °C (Saeed et al., 2015; Hu et al., 2021; El-Mir et al., 2022). Therefore, this paper studied the hydration mechanism and durability of LHCC used for dam concrete under 40 °C water curing through thermodynamic modeling and experiments. The resistance to chloride ion penetration, carbonation, and frost was evaluated through the RCM, accelerated carbonation, and rapid freeze–thaw cycle experiments, respectively. The hydration process was thermodynamically modeled by GEMS software, the generated crystal hydrate was analyzed by XRD, and the microstructure was examined by SEM and EDS.

Materials and methods

Raw materials

The cement was P I 42.5, which satisfied the quality requirements set out in Appendix A of GB8076-2008. The FA was Grade I. The purity of MEA was 87%, and its activity was 185 s according to the citric acid neutralization test. Classified as type M, it had a calcination temperature ranging from 900 °C to 1,100 °C. Table 1 and Figure 1 show the chemical compositions and particle size distributions of the raw materials, respectively.

Composition design of the cementitious materials

To reduce the heat of hydration and compensate for shrinkage as much as possible through expansion, the FA content in this study was set to 40%, and the content of MEA was set to 8% according to the mix proportion used in several previous projects. Meanwhile, the specimens in the study were cured in 40 °C water to match the temperature field inside the dam concrete. For a comparative study, the PC with the same water/binder was treated as the reference group. Table 2 indicates the compositions of cementitious materials used in the study.

Experimental methods

Chloride ion penetration experiment

In this study, the chloride ion penetration resistance was characterized by the chloride ion permeability coefficient through the rapid chloride ion migration coefficient (RCM) method. During the experiment, the specimens that were cured for 90 days were first placed in a vacuum water-retaining machine for 24 h and then in the test channel of the RCM-NTB chloride diffusion coefficient tester for another 24 h. Following the test, specimens were collected and split with a splitting tester. Finally, a 0.1 mol/L $AgNO_3$ solution was sprayed onto the split section of the specimens, and a vernier caliper was used to measure the distance between the color development boundary and the edge of the specimens. The area that is penetrated by chloride ions turned a silver white. The chloride diffusion coefficient was calculated by substituting the measured penetration depth into the related equations. Three specimens were tested for each group, and the average was used.

Carbonation experiment

In this study, the accelerated carbonation process was simulated on the carbonation test chamber with a carbon dioxide concentration of (20 ± 3)% and a relative humidity of 70 ± 5%. Prior to the experiment, the specimens that were cured for 90 days were placed in the oven at 60 °C and baked to a constant weight. The

TABLE 1 Chemical compositions of the raw materials (%).

Raw material	SiO_2	Al_2O_3	Fe_2O_3	CaO	MgO	SO_3	f-CaO	LOI
PC	20.08	5.09	3.81	63.41	2.06	2.33	0.88	1.72
FA	38.00	37.70	4.97	6.35	0.873	-	-	5.71
MEA	1.64	1.25	2.51	2.68	87	-	-	3.82

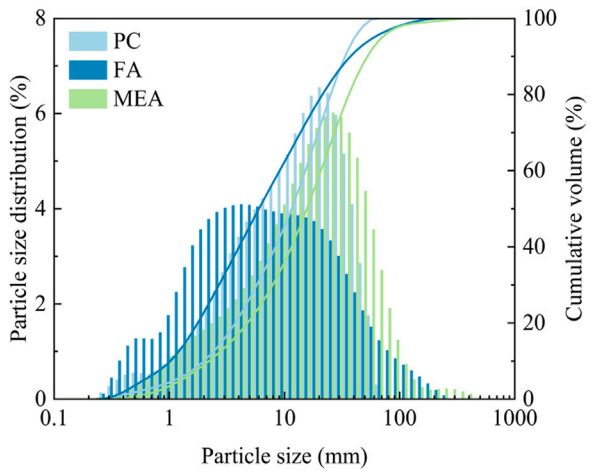

FIGURE 1
Particle size distributions of the raw materials.

TABLE 2 Compositions of cementitious materials (%).

Number	PC (%)	FA (%)	MEA (%)	Water (%)
PC	100	0	0	40
LHCC	60	40	8	40

specimens were then taken out after being carbonized for 3 days, 7 days, 14 days, and 28 days, respectively, and then split using an automatic testing machine. The phenolphthalein alcohol solution with a concentration of 1% was sprayed onto the cross section. There was no color change observed in the carbonized area, and it turned purple red in the non-carbonized area. After the color development was stabilized, a vernier caliper was used to measure the depth of the area without color change. Finally, the average was obtained from the measurement results of each side to characterize the carbonation.

The freeze–thaw cycle experiment

In this study, specimens cured to 90 days were placed on the concrete rapid freeze–thaw test machine after the initial mass was weighed and the initial relative dynamic elastic modulus was measured with a non-metallic ultrasonic detector. Specimens were collected after every 25 cycles to measure the mass and relative dynamic elastic modulus. When the mass loss rate reached 5% or the relative dynamic elastic modulus decreased by 60%, the freeze–thaw cycle experiment was terminated, and the maximum number of cycles was 200.

TABLE 3 Empirical reaction rate coefficients for the MPK model.

Phase	K_1	N_1	K_2	K_3	N_3	H
C_3S	1.500	.700	.050	1.100	3.300	2.000
C_2S	.500	1.000	.020	.700	5.000	1.550
C_3A	1.000	.850	.040	1.000	3.200	1.800
C_4AF	.370	.700	.015	.400	3.700	1.650
SiO_2	.490	.626	.047	.362	3.988	1.040
CaO	1.000	1.700	2.000	.239	.980	.010
Al_2O_3	.500	.702	.050	.393	2.000	.090

Thermodynamic modeling

Based on the Gibbs free energy minimization theory, the GEMS software was applied to calculate the equilibrium state of the system under specific conditions to simulate the hydration process of cement (Lothenbach et al., 2008; Carriço et al., 2020). To make the model applicable to the cement-based system containing FA, the modified Parrot–Kiloh model (MPK model) proposed by Glosser et al. was used and the specific form and parameters are shown in Eqs 1–6 (Glosser et al., 2020). The thermodynamic data on each phase were collected from Cemdata 18. Table 3 lists the reaction rate coefficients used in this study (Lothenbach et al., 2019).

$$\alpha(t) = \int_0^t DoR^* \left(\min\left\{ \frac{A}{A_0} r_1 r_2 r_3 \right\} f_{w/b} \beta_H e^{\left(\frac{E_i}{R} \left(\frac{1}{T_0} - \frac{1}{T} \right) \right)} \right) dt, \quad (1)$$

$$r_1 = \frac{K_1}{N_1} (1 - \alpha(t)) (-\ln(1 - \alpha(t)))^{1 - N_1}, \quad (2)$$

$$r_2 = \frac{K_2 \sqrt[3]{(1 - \alpha(t)2}}{1 - \sqrt[3]{(1 - \alpha(t))}}, \quad (3)$$

$$r_3 = K_3 (1 - \alpha(t))^{N_3}, \quad (4)$$

$$f_{w/b} = \left(1 + 3.33 \times \left(H \times \frac{w}{b} - \alpha_t \right) \right)^4, \quad (5)$$

$$\beta_H = \left[\frac{h - 0.55}{0.45} \right]^4, \quad (6)$$

where r_1, r_2, and r_3 are the rates of nucleation, precipitation, and diffusion, respectively; A and A_0 are the surface area and the reference surface area of cementitious material, respectively; R (8.314 J/mol/K) is the universal gas constant; E_i (J/mol) is the activation energy of each phase; T_0 and T are the reference temperature (298.15 K) and the

TABLE 4 Chloride ion penetration experiment results.

Number	Experimental temperature (K)	Penetration depth (m)
PC	301.5	0.0062
LHCC	301.2	0.0030

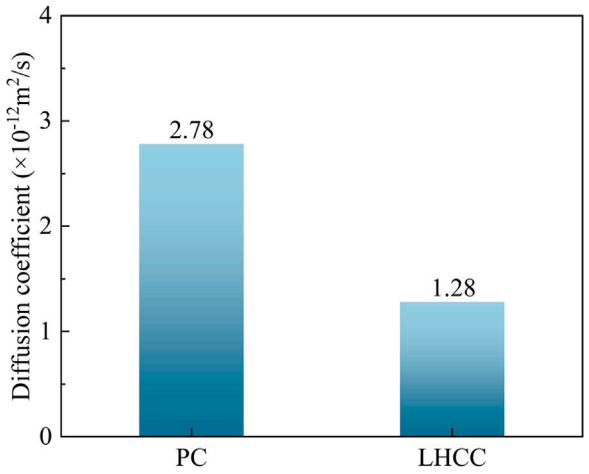

FIGURE 2
Chloride ion permeability coefficients of PC and LHCC.

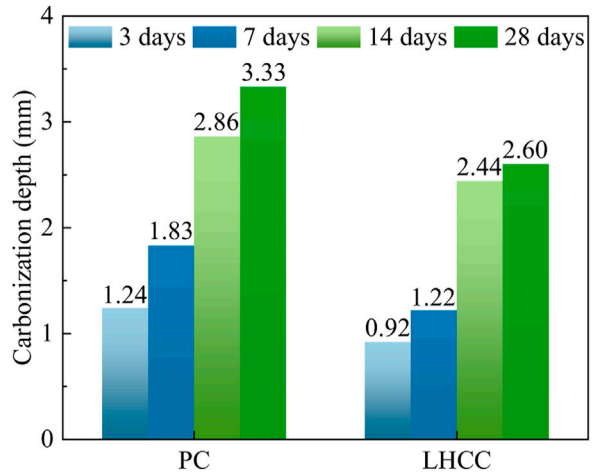

FIGURE 3
Carbonation depths of PC and LHCC.

modeling temperature, respectively; K_1, N_1, K_2, K_3, and N_3 are the parameters of the reaction rate; $\alpha(t)$ is the hydration degree of each phase; $f_{w/b}$ is the physical quantity affected by the water/binder w/b; H is a fitting factor; α_t is the average reaction degree at time t , $\alpha_t > H \times w/b$; and β_H is the physical quantity considering the influence of relative humidity h and generally takes 1.

X-ray diffraction (XRD)

To verify the accuracy of the GEMS simulation and to further understand the hydration process, XRD was used to analyze the generated crystal hydrate. The core of the broken specimen was immersed in isopropyl alcohol for 7 days and then dried in a vacuum drying oven at 60°C for 3 days to stop hydration. Before testing, the treated sample was ground into a powder and passed through a 200-mesh sieve. Finally, the prepared powder was used to obtain the XRD pattern with the equipment Bruker D8 advance at a scanning speed of 5°/min, within the scanning range of 5°–70°.

Scanning electron microscopy (SEM) and energy dispersive spectrometry (EDS)

To further understand the hydration mechanism of LHCC, the microstructure of the hardened paste was examined under SEM and EDS. A small amount of samples that have stopped hydration directly stuck to the conductive adhesive, while gold was sprayed with an Oxford Quorum SC7620 sputtering coater for 45 s. Subsequently, the TESCAN MIRA LMS device was used to examine the morphology of the sample with an acceleration voltage set to 3 kV. When shooting the energy spectrum, the acceleration voltage was 15 kV and the detector was the SE2.

Results and discussion

Durability

Chloride ion penetration resistance

Table 4 lists the experimental temperature and penetration depth, as measured during the RCM experiment. By inputting the relevant data into Eqs (7) and (8), the chloride ion diffusion coefficients of PC and LHCC that were cured to 90 days were calculated and the results are shown in Figure 2.

$$D_{RCM} = 2.872 \times 10^{-6} \frac{Th(X_d - \alpha\sqrt{X_d})}{t}, \quad (7)$$

$$\alpha = 3.338 \times 10^{-3} \sqrt{Th}, \quad (8)$$

where D_{RCM} is the chloride ion diffusion coefficient; T is the experiment temperature (K); h is the height of the specimen (m); X_d is the chloride ion diffusion depth (m); t is the power on time (s); and α is an auxiliary variable.

The figure shows that the D_{RCM} of PC was 2.78×10^{-12} m^2/s and the D_{RCM} of LHCC was 1.28×10^{-12} m^2/s. The D_{RCM} of LHCC was about 46% of that of the PC, which suggests a stronger resistance to chloride ion penetration. As the particle size of the FA used was smaller than the cement clinker, the pores of the cementitious matrix could be filled with FA and thus complicating the pore structure of the hardened paste. This hindered the movement of chloride ions in the

TABLE 5 Mass loss rates during 200 freeze–thaw cycles (%).

Number	Number of cycles								
	0	25	50	75	100	125	150	175	200
PC	0	0.2	0.5	0.7	1.7	2.4	4.8		
LHCC	0	0.1	0.3	0.5	0.9	1.8	2.2	3.5	4.5

TABLE 6 Relative dynamic elastic modulus during 200 freeze and thaw cycles (%).

Number	Number of cycles								
	0	25	50	75	100	125	150	175	200
PC	100	99.2	97.0	92.5	81.8	72.5	43.8		
LHCC	100	99.5	97.8	97.3	92.3	80.5	76.3	65.4	55.1

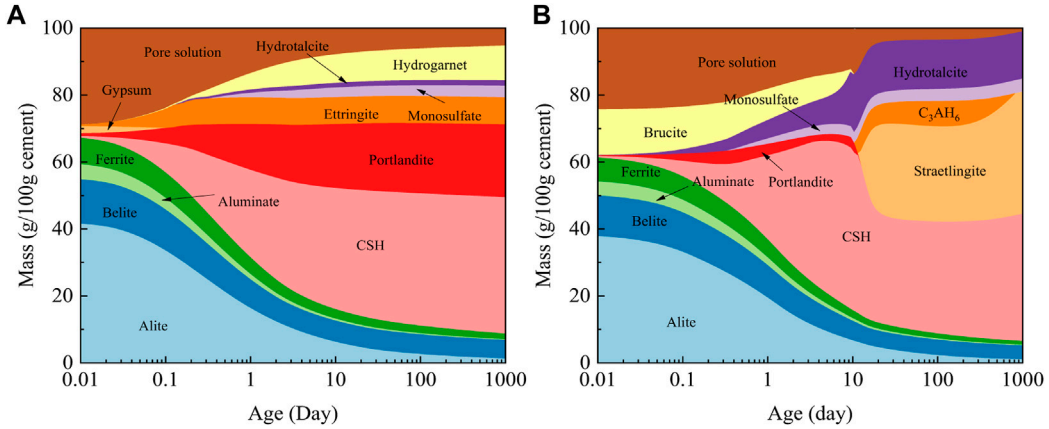

FIGURE 4
Phase evolution of **(A)** PC and **(B)** LHCC by thermodynamic simulation.

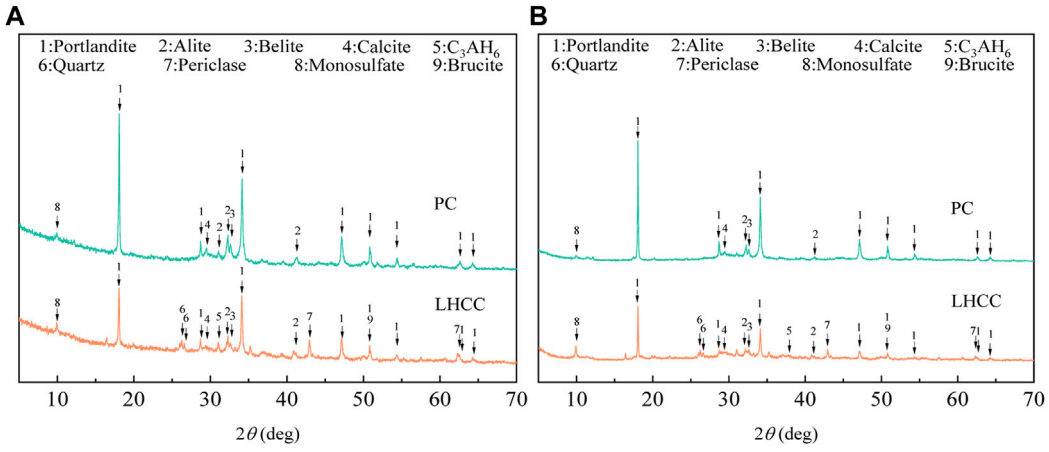

FIGURE 5
XRD spectra of specimens cured for **(A)** 3 days and **(B)** 90 days.

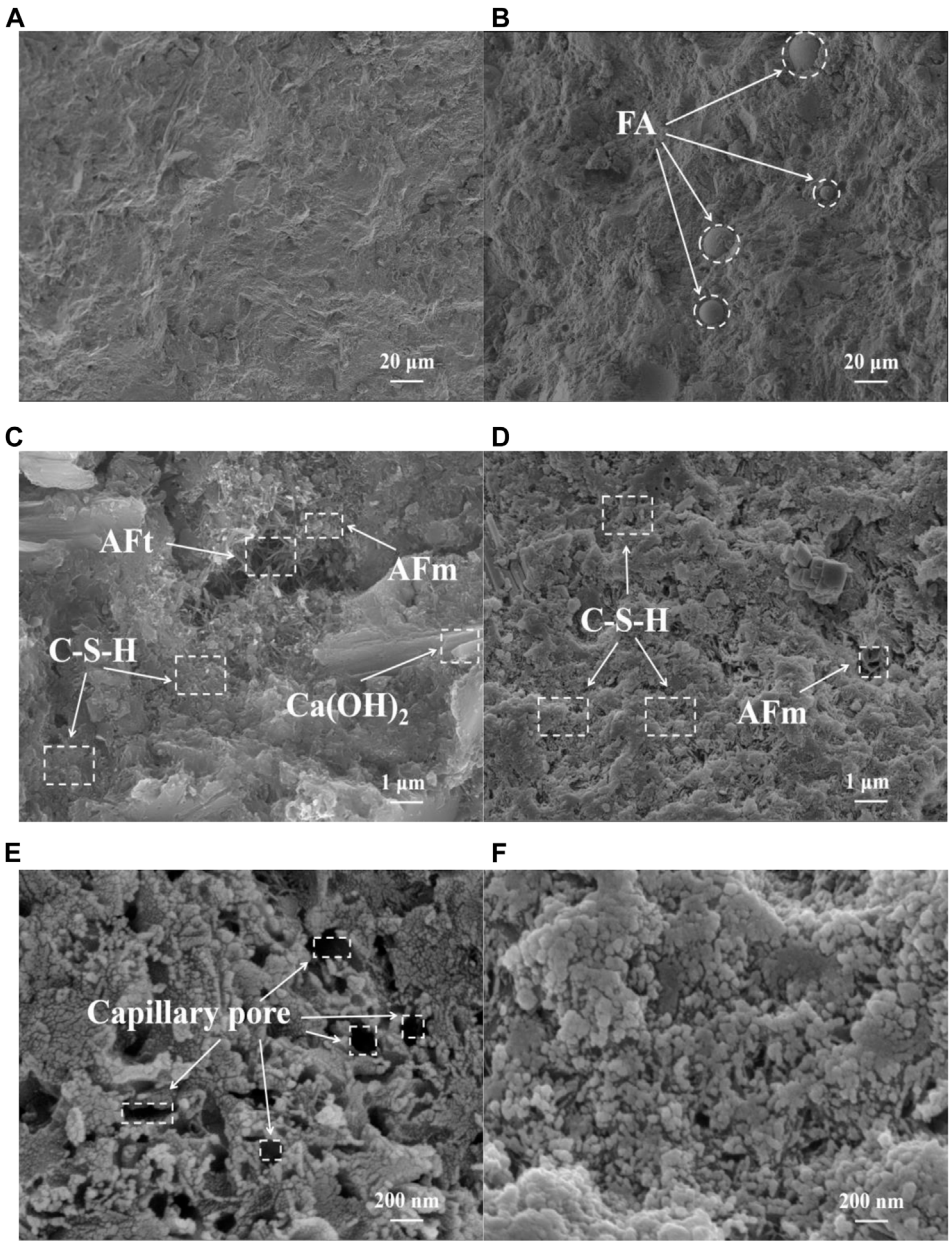

FIGURE 6
Comparison of the micromorphology of **(A), (C),** and **(E)** PC and **(B), (D),** and **(F)** LHCC cured for 90 days.

pores and blocked the diffusion channel of the free chloride ions in the cement. In the meantime, the $Mg(OH)_2$ generated from MgO hydration continuously reduced the pore volume through delayed expansion, which reduced the number of diffusion channels for chloride ions (Pu and Unluer, 2018). In the follow-up study, the enhancement of chloride ion penetration resistance was further discussed in combination with the phase evolution output through the thermodynamic model and the SEM observation results.

Carbonation resistance

Figure 3 displays the carbonation depths of PC and LHCC that were cured to 90 days in the accelerated carbonation experiment. The carbonation depths of the PC were 1.24 mm, 1.83 mm, 2.86 mm, and 3.33 mm at the carbonation age of 3 days, 7 days, 14 days, and 28 days, respectively. In addition, the LHCC at the same carbonation age were 0.92 mm, 1.22 mm, 2.44 mm, and 2.60 mm. In comparison, the carbonation depth of the PC at each carbonized age was greater than the LHCC. Meanwhile, the carbonation resistance of LHCC at 3 days, 7 days, 14 days, and 28 days was 25.8%, 33.3%, 14.7%, and 21.9% higher than that of PC at the same age, respectively. Both the micro-filling effect of FA and the delay expansion of $Mg(OH)_2$ significantly improved the carbonation resistance of cementitious composites (Choi et al., 2014). According to previous studies, $Mg(OH)_2$ generated dense $CaCO_3$ and $MgCO_3$ through a carbonation reaction in the early stage, whose reactions are shown in Eqs 9–11. $MgCO_3$ developed a network and prismatic microstructure, which was filled in the cementitious matrix and thus

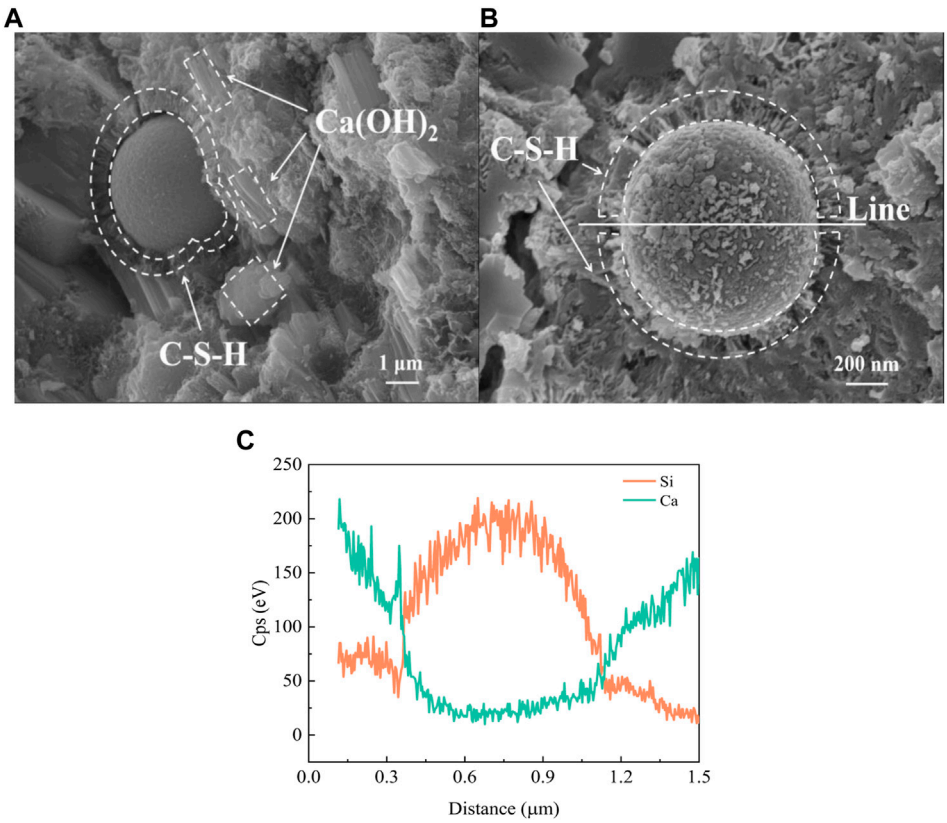

FIGURE 7
Spherical vitreous morphology of FA in LHCC under **(A)** 20,000x and **(B)** 50,000x **(C)** element line scanning in **(B)**.

improved the density of the cement. Consequently, it became increasingly difficult for the external carbon dioxide to diffuse to the area to be carbonized (Liska et al., 2008). The exact mechanism of the smaller scale will be discussed later.

$$Mg(OH)_2+CO_2+H_2O \rightarrow MgCO_3 \cdot 3H_2O \quad (9)$$

$$5Mg(OH)_2+4CO_2 \rightarrow 4MgCO_3 \cdot Mg(OH)_2 \cdot 4H_2O \quad (10)$$

$$5Mg(OH)_2+4CO_2 + H_2O \rightarrow 4MgCO_3 \cdot Mg(OH)_2 \cdot 5H_2O \quad (11)$$

Frost resistance

Table 5 and Table 6 show the mass loss rate and relative dynamic elastic modulus of PC and LHCC that were cured to 90 days in the freeze–thaw cycle experiment, respectively. As shown in these two tables, PC and LHCC withstood 150 and 200 freeze–thaw cycles, respectively. Meanwhile, LHCC had a smaller mass loss rate and larger relative dynamic elastic modulus than PC after the same number of freeze–thaw cycles. As a consequence, LHCC performed better in frost resistance. When the water trapped by the pores inside the cement paste was frozen, the volume expanded in this part and thus pushed the non-frozen water in the pores around to generate hydrostatic pressure. This was the cause for the freeze–thaw damage. Because of the delayed expansion of $Mg(OH)_2$, there was a reduction in the volume that could hold the pore solution. As a result, the maximum hydrostatic pressure declined and the rate of freeze–thaw damage decreased. For the additional mechanism of improving the frost resistance of LHCC, it will be further elaborated later.

Hydration process

Figure 4 shows the phase evolution of hydrated pastes during 1,000 days, as calculated through the thermodynamic simulation of GEMS software. With the hydration extension, the clinker in PC progressively decreased and the order of the reaction rates was as follows: aluminate > alite > ferrite > belite. The hydration products of PC were dominated by portlandite, C-S-H, and ettringite and the content gradually increased. Therefore, the number largely determined the performance of the hardened cement paste. Meanwhile, as the consumption of the pore solution continued, the capillary negative pressure in the pores caused the hardened cement paste to shrink gradually or even crack. By providing channels for the diffusion of chloride ions, carbon dioxide, and water, this hindered the improvement of the durability.

With the introduction of FA in large amounts, the initial content of clinker in the LHCC decreased, as a result of which the C-S-H and portlandite generated in the early stage were outweighed by PC. MEA was mostly hydrated to brucite first, and the expansion effect compensated for the significant shrinkage occurring in the early stage of hydration. This was the requisite for the enhancement of durability (Song et al., 2021). As hydration proceeded, portlandite and brucite continued to accumulate. When the environmental alkalinity was sufficient to stimulate the

pozzolanic activity of FA, the aluminosilicate in FA reacted with portlandite to generate C-S-H and C_3AH_6, which continuously reduced portlandite and greatly increased C-S-H (Deschner et al., 2012; Hamzaoui et al., 2016). Meanwhile, C-S-H generated from the secondary hydration of cement was further stabilized to hinder carbonization and indicated the formation of stronger carbonization resistance (Ali and Mullick, 1998; Qian et al., 1998). The low availability of CaO caused more stratlingite to be generated in the later hydration stage of LHCC, a kind of AFm phase, which is often incompatible with portlandite. In addition, brucite partially reacted with the aluminates in FA to generate hydrotalcite that was capable of absorbing free chloride ions and thus enhanced the resistance to chloride ion penetration of LHCC to a significant extent (Yang et al., 2020).

Figure 5 shows the XRD patterns of PC and LHCC that were cured for 3 and 90 days. The addition of FA to replace part of the cement reduced the content of portlandite and generated C_3AH_6 in the later stage. Meanwhile, the content of brucite in LHCC decreased with age, which was consistent with the simulation results of GEMS software. Due to the characteristics of the gel, the peak position of C-S-H could not be identified by XRD. In addition, compared with PC, there were more monosulfates in LHCC.

Microstructural characteristics

To a large extent, the macroscopic properties of cement-based materials depend on the spatial aggregates formed by the mutual accumulation and connection of their hydration products. To better analyze the mechanism of the difference in durability between the two, Figure 6 shows the micromorphology of PC and LHCC at different scales. When the magnification was 1,000, it was obvious in LHCC that the spherical particles in the FA were closely embedded in the cementitious matrix, which produced the micro-filling effect. When the magnification was 10,000, there were more layered large crystals of $Ca(OH)_2$ stacked in the PC and overlapped with C-S-H to form a space grid, and the pores were filled with plenty of AFt and AFm. However, at the same magnification, it was difficult to find oriented $Ca(OH)_2$ layered crystals in LHCC, and the hydration products were dominated by C-S-H, which was consistent with the phase evolution output from the thermodynamic model. Figure 6 e) and f) show the morphology of C-S-H, as observed in PC and LHCC at 50,000 magnifications, respectively. The connection among C-S-H in PC was weak with a distribution of many capillary pores, which was suspected to occur from the contraction caused by negative capillary pressure (Ahmad et al., 2019). According to some research, the existence of capillary pores was adverse to the development of mechanical properties and the improvement of durability (Li and Li, 2014; Pu et al., 2021). In contrast, the network structure formed by C-S-H overlapping in LHCC was denser and extensively distributed. On the one hand, the delay in the expansion of $Mg(OH)_2$ was conducive to compensating for the shrinkage of cement. On the other hand, the existence of FA caused the secondary hydration of cement. Therefore, due to the combined effect of MEA and FA, more C-S-H was filled in the capillary pore volume, which improved the compactness of the pore structure for hardened paste and enhanced its resistance to penetration of chloride ions, carbon dioxide, and water.

The hydration degree of large amounts of FA in cement is a long-standing concern. If there is no way to control the inert filling effect of FA, it is difficult to ensure the effect of cement secondary hydration. Figure 7 shows the spherical vitreous morphology of FA in LHCC. The spherical glass incorporated into the cement matrix reacted at a slow pace with the surrounding $Ca(OH)_2$ to generate fibrous hydrate, as shown in Figure 7 b). The result of element line scanning in Figure 7 c) and the morphology of the hydrate jointly indicated that the fibrous hydrate was C-S-H, which indicated that FA in LHCC could effectively participate in the hydration (Richardson, 2004; Deschner et al., 2012). In addition to the alkaline products obtained by the hydration of PC, the excitation of pozzolanic activity of FA was also promoted by the alkaline environment created by $Mg(OH)_2$ in LHCC and high-temperature curing (Liu and Zhang, 2021). The increasing hydration degree of FA enhanced the mass generation of C-S-H and improved the outcome of pore size refinement. This significantly reduced the diffusion of the pore solution, mitigated the mass loss caused by the frost heaving force and decreased the relative dynamic elastic modulus. Apart from strengthening the connection between the spherical glass body and the surrounding cement matrix, the fibrous C-S-H generated by the hydration of FA also filled the porous cement matrix, which was beneficial to the improvement of crack resistance and durability for dam concrete.

Conclusion

Thermodynamic modeling and experiments were performed in this paper to systematically explore the hydration mechanism and durability of LHCC used for dam concrete under 40 °C water curing. The conclusions obtained in this study are as follows.

1 Compared with PC, LHCC performs better in resistance to chloride ion penetration, carbonation, and frost, which demonstrates the excellent durability of LHCC.
2 With the decrease of portlandite content, there is compensation for the content of C-S-H and stratlingite in LHCC, which results from the pozzolanic reaction of FA. There are plenty of hydration products generated in the later stage to fill the pores caused by cement shrinkage. Meanwhile, hydrotalcite, which can absorb chloride ions, is generated and steadily increases.
3 The microstructure of LHCC is dominated by C-S-H that is overlapping and closely arranged with almost no capillary pores observed. In addition, the fibrous C-S-H formed by the hydration of FA in LHCC strengthens the connection between the spherical vitreous and the surrounding cementitious matrix to fill the porous cement matrix.

Data availability statement

The original contributions presented in the study are included in the article/supplementary material, and further inquiries can be directed to the corresponding author.

Author contributions

JZ: investigation, methodology, project administration, and writing—original draft. TL: experimental design, data analysis, writing—original draft, and supervision.

Conflict of interest

The authors declare that the research was conducted in the absence of any commercial or financial relationships that could be construed as a potential conflict of interest.

Publisher's note

References

Ahmad, M. R., Chen, B., and Yu, J. (2019). A comprehensive study of basalt fiber reinforced magnesium phosphate cement incorporating ultrafine fly ash. *Compos. Part B Eng.* 168, 204–217. doi:10.1016/j.compositesb.2018.12.065

Ali, M. M., and Mullick, A. K. (1998). Volume stabilisation of high MgO cement: Effect of curing conditions and fly ash addition. *Cem. Concr. Res.* 28 (11), 1585–1594. doi:10.1016/S0008-8846(98)00140-9

Atiş, C. D. (2002). Heat evolution of high-volume fly ash concrete. *Cem. Concr. Res.* 32 (5), 751–756. doi:10.1016/S0008-8846(01)00755-4

Cao, B., and Al-Tabbaa, A. (2022). Reactive MgO-based self-healing slag-cement-bentonite slurry walls. *Cem. Concr. Compos.* 131, 104565. doi:10.1016/j.cemconcomp.2022.104565

Carriço, A., Bogas, J. A., and Guedes, M. (2020). Thermoactivated cementitious materials – a review. *Constr. Build. Mater.* 250, 118873. doi:10.1016/j.conbuildmat.2020.118873

Chen, Y.-Y., Chen, S.-Y., Yang, C.-J., and Chen, H.-T. (2017). Effects of insulation materials on mass concrete with pozzolans. *Constr. Build. Mater.* 137, 261–271. doi:10.1016/j.conbuildmat.2017.01.059

Choi, S.-w., Jang, B.-s., Kim, J.-h., and Lee, K.-m. (2014). Durability characteristics of fly ash concrete containing lightly-burnt MgO. *Constr. Build. Mater.* 58, 77–84. doi:10.1016/j.conbuildmat.2014.01.080

Deschner, F., Winnefeld, F., Lothenbach, B., Seufert, S., Schwesig, P., Dittrich, S., et al. (2012). Hydration of Portland cement with high replacement by siliceous fly ash. *Cem. Concr. Res.* 42 (10), 1389–1400. doi:10.1016/j.cemconres.2012.06.009

Dung, N. T., and Unluer, C. (2021). Advances in the hydration of reactive MgO cement blends incorporating different magnesium carbonates. *Constr. Build. Mater.* 294, 123573. doi:10.1016/j.conbuildmat.2021.123573

El-Mir, A., Assaad, J. J., Nehme, S. G., and El-Hassan, H. (2022). Correlating strength and durability to time-temperature profiles of high-performance mass concrete. *Case Stud. Constr. Mater.* 16, e01055. doi:10.1016/j.cscm.2022.e01055

Gao, P.-w., Xu, S.-y., Chen, X., Li, J., and Lu, X.-l. (2013). Research on autogenous volume deformation of concrete with MgO. *Constr. Build. Mater.* 40, 998–1001. doi:10.1016/j.conbuildmat.2012.11.025

Gao, P., Lu, X., Geng, F., Li, X., Hou, J., Lin, H., et al. (2008). Production of MgO-type expansive agent in dam concrete by use of industrial by-products. *Build. Environ.* 43 (4), 453–457. doi:10.1016/j.buildenv.2007.01.037

Glosser, D., Suraneni, P., Isgor, O. B., and Weiss, W. J. (2020). Estimating reaction kinetics of cementitious pastes containing fly ash. *Cem. Concr. Compos.* 112, 103655. doi:10.1016/j.cemconcomp.2020.103655

Ha, J.-H., Jung, Y. s., and Cho, Y.-g. (2014). Thermal crack control in mass concrete structure using an automated curing system. *Automation Constr.* 45, 16–24. doi:10.1016/j.autcon.2014.04.014

Hamzaoui, R., Bouchenafa, O., Guessasma, S., Leklou, N., and Bouaziz, A. (2016). The sequel of modified fly ashes using high energy ball milling on mechanical performance of substituted past cement. *Mater. Des.* 90, 29–37. doi:10.1016/j.matdes.2015.10.109

Hu, Y., Chen, J., Zou, F., He, M., Mao, J., Liu, X., et al. (2021). A comparative study of temperature of mass concrete placed in August and November based on on-site measurement. *Case Stud. Constr. Mater.* 15, e00694. doi:10.1016/j.cscm.2021.e00694

Klemczak, B., Batog, M., Pilch, M., and Żmij, A. (2017). Analysis of cracking risk in early age mass concrete with different aggregate types. *Procedia Eng.* 193, 234–241. doi:10.1016/j.proeng.2017.06.209

Li, Y., and Li, J. (2014). Capillary tension theory for prediction of early autogenous shrinkage of self-consolidating concrete. *Constr. Build. Mater.* 53, 511–516. doi:10.1016/j.conbuildmat.2013.12.010

Liska, M., Vandeperre, L. J., and Al-Tabbaa, A. (2008). Influence of carbonation on the properties of reactive magnesia cement-based pressed masonry units. *Adv. Cem. Res.* 20 (2), 53–64. doi:10.1680/adcr.2008.20.2.53

Liu, C., and Zhang, M. (2021). Effect of curing temperature on hydration, microstructure and ionic diffusivity of fly ash blended cement paste: A modelling study. *Constr. Build. Mater.* 297, 123834. doi:10.1016/j.conbuildmat.2021.123834

Lothenbach, B., Kulik, D. A., Matschei, T., Balonis, M., Baquerizo, L., Dilnesa, B., et al. (2019). Cemdata18: A chemical thermodynamic database for hydrated Portland cements and alkali-activated materials. *Cem. Concr. Res.* 115, 472–506. doi:10.1016/j.cemconres.2018.04.018

Lothenbach, B., Matschei, T., Möschner, G., and Glasser, F. P. (2008). Thermodynamic modelling of the effect of temperature on the hydration and porosity of Portland cement. *Cem. Concr. Res.* 38 (1), 1–18. doi:10.1016/j.cemconres.2007.08.017

Mo, L., Deng, M., Tang, M., and Al-Tabbaa, A. (2014). MgO expansive cement and concrete in China: Past, present and future. *Cem. Concr. Res.* 57, 1–12. doi:10.1016/j.cemconres.2013.12.007

Ng, S., and Justnes, H. (2016). Influence of plasticizers on the rheology and early heat of hydration of blended cements with high content of fly ash. *Cem. Concr. Compos.* 65, 41–54. doi:10.1016/j.cemconcomp.2015.10.005

Noroozi, A. G., Ajalloeian, R., and Bayat, M. (2022). Experimental study of the role of interface element in Earth dams with asphalt concrete core - case study: Mijran dam. *Case Stud. Constr. Mater.* 16, e01004. doi:10.1016/j.cscm.2022.e01004

Pu, L., and Unluer, C. (2018). Durability of carbonated MgO concrete containing fly ash and ground granulated blast-furnace slag. *Constr. Build. Mater.* 192, 403–415. doi:10.1016/j.conbuildmat.2018.10.121

Pu, S., Zhu, Z., Song, W., Huo, W., and Zhang, J. (2021). Mechanical and microscopic properties of fly ash phosphoric acid-based geopolymer paste: A comprehensive study. *Constr. Build. Mater.* 299, 123947. doi:10.1016/j.conbuildmat.2021.123947

Qian, G., Xu, G., Li, H., and Li, A. (1998). The effect of autoclave temperature on the expansion and hydrothermal products of high-MgO blended cements 11Communicated by V. Johansen. *Cem. Concr. Res.* 28 (1), 1–6. doi:10.1016/s0008-8846(97)00202-0

Richardson, I. G. (2004). Tobermorite/jennite- and tobermorite/calcium hydroxide-based models for the structure of C-S-H: Applicability to hardened pastes of tricalcium silicate, β-dicalcium silicate, Portland cement, and blends of Portland cement with blast-furnace slag, metakaolin, or silica fume. *Cem. Concr. Res.* 34 (9), 1733–1777. doi:10.1016/j.cemconres.2004.05.034

Saeed, M. K., Rahman, M. K., and Baluch, M. H. (2015). Early age thermal cracking of mass concrete blocks with Portland cement and ground granulated blast-furnace slag. *Mag. Concr. Res.* 68 (13), 647–663. doi:10.1680/jmacr.15.00044

Song, Q., Su, J., Nie, J., Li, H., Hu, Y., Chen, Y., et al. (2021). The occurrence of MgO and its influence on properties of clinker and cement: A review. *Constr. Build. Mater.* 293, 123494. doi:10.1016/j.conbuildmat.2021.123494

Tayade, K. C., Deshpande, N. V., and Pofale, A. D. (2014). Experimental study of temperature rise of concrete and assessment of cracking due to internal restraint. *Int. J. Civ. Struct. Eng.* 4 (3), 353–364.

Vargas, J., and Halog, A. (2015). Effective carbon emission reductions from using upgraded fly ash in the cement industry. *J. Clean. Prod.* 103, 948–959. doi:10.1016/j.jclepro.2015.04.136

Wang, L., Guo, F., Lin, Y., Yang, H., and Tang, S. W. (2020). Comparison between the effects of phosphorous slag and fly ash on the C-S-H structure, long-term hydration heat and volume deformation of cement-based materials. *Constr. Build. Mater.* 250, 118807. doi:10.1016/j.conbuildmat.2020.118807

Wang, L., Yang, H. Q., Zhou, S. H., Chen, E., and Tang, S. W. (2018). Mechanical properties, long-term hydration heat, shinkage behavior and crack resistance of dam concrete designed with low heat Portland (LHP) cement and fly ash. *Constr. Build. Mater.* 187, 1073–1091. doi:10.1016/j.conbuildmat.2018.08.056

Wolterbeek, T. K. T., Cornelissen, E. K., Hangx, S. J. T., and Spiers, C. J. (2021). Impact of downhole pressure and fluid-access on the effectiveness of wellbore cement expansion additives. *Cem. Concr. Res.* 147, 106514. doi:10.1016/j.cemconres.2021.106514

Xin, J., Zhang, G., Liu, Y., Wang, Z., and Wu, Z. (2018). Effect of temperature history and restraint degree on cracking behavior of early-age concrete. *Constr. Build. Mater.* 192, 381–390. doi:10.1016/j.conbuildmat.2018.10.066

Yang, T., Zhang, Z., Zhang, F., Gao, Y., and Wu, Q. (2020). Chloride and heavy metal binding capacities of hydrotalcite-like phases formed in greener one-part sodium carbonate-activated slag cements. *J. Clean. Prod.* 253, 120047. doi:10.1016/j.jclepro.2020.120047

Yoon, Y.-S., Won, J.-P., Woo, S.-K., and Song, Y.-C. (2002). Enhanced durability performance of fly ash concrete for concrete-faced rockfill dam application. *Cem. Concr. Res.* 32 (1), 23–30. doi:10.1016/S0008-8846(01)00623-8

Zhang, J., Lv, T., Han, Q., Zhu, Y., Hou, D., and Dong, B. (2022). Effects of fly ash on MgO-based shrinkage-compensating cement: Microstructure and properties. *Constr. Build. Mater.* 339, 127648. doi:10.1016/j.conbuildmat.2022.127648

Zhang, J. (2022). Recent advance of MgO expansive agent in cement and concrete. *J. Build. Eng.* 45, 103633. doi:10.1016/j.jobe.2021.103633

Zhang, M. H., and Canmet (1995). Microstructure, crack propagation, and mechanical properties of cement pastes containing high volumes of fly ashes. *Cem. Concr. Res.* 25 (6), 1165–1178. doi:10.1016/0008-8846(95)00109-P

Zheng, F., Hong, S., Hou, D., Dong, B., Kong, Z., and Jiang, R. (2022). Rapid visualization and quantification of water penetration into cement paste through cracks with X-ray imaging. *Cem. Concr. Compos.* 125, 104293. doi:10.1016/j.cemconcomp.2021.104293